THE JOURNAL OF PHYSICAL CHEMISTRY C
A JOURNAL OF THE AMERICAN CHEMICAL SOCIETY

pubs.acs.org/JPCC

Article

Luminescence Tuning of NIR Luminescence Nanophosphor Bi^{3+}/Yb^{3+}-Doped RE_2MoO_6 (RE = Gd, Y, and Lu) and $Gd_2Mo_{1-x}W_xO_6$

Taisei Hangai, Takuya Hasegawa,* Jian Xu, Takayuki Nakanishi, Takashi Takeda, Tomoyo Goto, Yasushi Sato, Ayahisa Okawa, and Shu Yin

Cite This: J. Phys. Chem. C 2024, 128, 20360−20368

Read Online

ACCESS | Metrics & More | Article Recommendations | Supporting Information

ABSTRACT: Near-infrared nanophosphors have attracted attention due to their wide application fields, including component analysis, bioimaging, and spectral converters of sunlight for crystalline silicon solar cells (c-Si). Yb^{3+} ions exhibit near-infrared (NIR) luminescence at around 1000 nm, which is consistent with the first biological window and the maximum responsivity range of c-Si. Therefore, we focused on and successfully synthesized Bi^{3+}/Yb^{3+}-doped NIR luminescence nanophosphors, RE_2MoO_6:Bi^{3+},Yb^{3+} (RE=Gd, Y, and Lu) and $Gd_2Mo_{1-x}W_xO_6$:Bi^{3+},Yb^{3+} (x = 0−0.5), utilizing a solvothermal reaction process. All samples exhibit NIR luminescence of Yb^{3+} ions under ultra-violet (UV) light excitation and broadband excitation due to the charge transfer transition between the O 2p/Bi 6s and Mo 4d or W 5d orbitals, indicated by their optical properties of photoluminescence (PL), PL excitation (PLE), and reflectance spectra. Furthermore, to evaluate the contribution of the Gd_2MoO_6:Bi,Yb (GMO:Bi,Yb) nanophosphor to the conversion efficiency of c-Si, a phosphor-converted film was made using dimethylpolysiloxane (PDMS) and the GMO:Bi,Yb nanophosphor. The results showed that the conversion efficiency of c-Si with the PDMS/GMO:Bi,Yb film is higher than that of c-Si with the PDMS-only film. Based on these results, the utilization of down-shifting nanophosphors is able to enhance the conversion efficiency of c-Si, which could be beneficial in addressing future energy challenges.

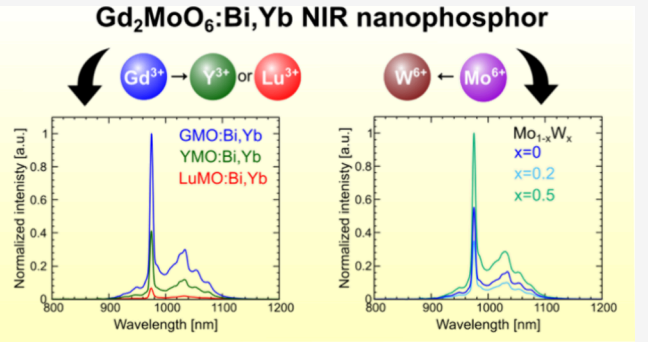

1. INTRODUCTION

Near-infrared (NIR) light, defined as the wavelength range from 700 to 1400 nm,[1] plays a crucial role in many application fields due to its outstanding properties. For instance, NIR light is absorbed by specific molecules, enabling its use in component analysis and bioimaging.[2−4] These characteristics make NIR light indispensable in various scientific fields. Therefore, the development of near-infrared (NIR) phosphors is crucial. As NIR luminescence centers, many researchers have chosen lanthanide ions such as Eu^{2+} or transition metal ions like Cr^{3+} and Ni^{2+}.[5−7] However, the transition types of these ions (Eu^{2+}: 4f-5d transitions; and Cr^{3+}, Ni^{2+}: 3d-3d transitions) affect their coordination environment. Consequently, an appropriate host matrix must be selected for these ions to exhibit NIR luminescence, which greatly limits the range of the host matrix selection. This represents a significant challenge in current NIR phosphor research. Lanthanide ions such as Yb^{3+}, Nd^{3+}, and Er^{3+} possess an attractive property of showing NIR luminescence regardless of the host matrix due to their 4f-4f intratransitions.[8−10] Specifically, Yb^{3+} ions exhibit a single energy level transition of $^2F_{5/2} \rightarrow {}^2F_{7/2}$, resulting in an emission around 1000 nm.[11,12] Their emission wavelength aligns perfectly with the first biological window, which is highly beneficial for bioimaging applications.[13] Furthermore, the emission wavelength of Yb^{3+} also matches the responsivity peak of silicon-based solar cells.[14] This alignment is expected to enhance the overall efficiency of solar cells by converting a broader spectrum of sunlight into usable energy. Given these characteristics, Yb^{3+} stands out as a highly promising ion for NIR luminescence applications.

However, despite these advantages, Yb^{3+} has a relatively low absorption coefficient due to its forbidden transitions. To improve the low absorption efficiency, it is desirable to apply an energy transfer process from parity/spin-allowed transitions with higher absorption efficiency than forbidden transition.[15] Recently, Ce^{3+} ions have often been utilized for the energy donor of Yb^{3+} because Ce^{3+} ions exhibit 4f-5d transition with allowed transition under ultra-violet (UV) light.[16,17] However, the total optical absorption coefficient is still low as the

Received: July 18, 2024
Revised: October 15, 2024
Accepted: October 16, 2024
Published: November 15, 2024

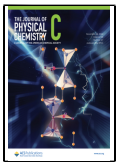

https://doi.org/10.1021/acs.jpcc.4c04814
J. Phys. Chem. C 2024, 128, 20360−20368

optimum doping concentrations of Ce^{3+} toward optimum emission intensity are only a few mol % in the matrix due to the concentration quenching effect, resulting in limited absorption. For instance, $CaSc_2O_4$:Ce^{3+} exhibits only a 3% reduction in reflectance due to the 4f-5d transition of Ce^{3+}, and in Ce^{3+}-doped $Ca_2YZr_2Al_3O_{12}$ garnet, the reflectance decreased by 10%, suggesting high possibility for enhancing the absorption efficiency.[18,19] Employing a ligand-to-metal charge transfer (LMCT) transition of the host matrix can overcome the issues of limited absorption efficiency from dopants because the transition utilizes the absorption of the host matrix rather than the dopant.[20] Therefore, the NIR phosphors showing LMCT transitions of the host matrix are expected to absorb sunlight more efficiently compared to the conventional Ce^{3+}-doped phosphors.

Our research has found that Yb^{3+}-doped Gd_2MoO_6 (GMO:Yb) nanophosphors are ideal for satisfying these conditions.[21] GMO:Yb nanophosphors exhibit a broad excitation band from 200 to 400 nm due to the LMCT transition between Mo and O atoms and demonstrate NIR luminescence of Yb^{3+} ions around 1000 nm under 363 nm excitation (Figure 1a), suggesting that they have a suitable

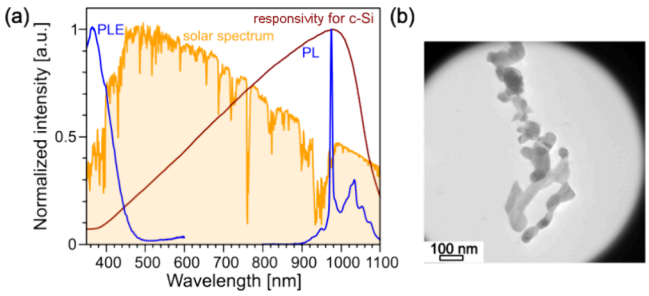

Figure 1. (a) PL (λ_{ex}= 363 nm)·PLE (λ_{em}= 975 nm) spectra for the GMO:Bi,Yb nanophosphor (blue), responsivity for c-Si (brown), and solar spectrum (orange). (b) TEM images for GMO:Bi,Yb nanophosphors.

spectral modification.[22] As shown in Figure 1b, they can be synthesized in a nanosize with around 50 nm of particle size using the solvothermal method; thus, the nanosized nature of these phosphors suppresses the scattering of visible light from sunlight, making them highly effective for solar energy applications.[23] Additionally, their small size is advantageous for bioimaging applications because nanoparticles can easily penetrate biological tissues and cells, providing enhanced imaging resolution and deeper tissue penetration compared to larger particles.[24]

Chemical composition adjustment plays a crucial role to investigate the properties of such an attractive material with excellent optical characteristics for the GMO:Bi,Yb nanophosphor, as the strategy effectively evaluates and enhances optical properties by modifying the coordination environment and electronic structure.[25−28] In the Gd_2MoO_6 matrix, the optical property can be modulated by substituting Gd and Mo sites with other rare earths (such as Y and Lu) and W ions. The Y_2MoO_6 and Lu_2MoO_6 matrices are isostructural with the monoclinic phase of Gd_2MoO_6,[29,30] enabling a systematic comparison and understanding of the substitution effect on optical properties. On the other hand, Gd_2WO_6 exhibits LMCT transitions between the O 2p and W 5d orbital,[31] which can significantly tune optical properties because GMO:Bi,Yb nanophosphors also utilize the LMCT transitions.

In this study, we synthesized and characterized the optical properties of the GMO:Bi,Yb family, including RE_2MoO_6:Bi,Yb (RE= Y, Lu) and $Gd_2Mo_{1-x}W_xO_6$:Bi,Yb (x = 0−1) nanophosphors. Additionally, GMO:Bi,Yb nanophosphor films were prepared in anticipation of their excellent optical properties, as shown in Figure 1a, and their effect on the conversion efficiency of solar cells was also evaluated. Focusing on the excellent permeability, flexibility, and stability of dimethylpolysiloxane (PDMS),[32] we prepared prototype films of phosphors encapsulated in PDMS. This study provides insights into the development of novel near-infrared phosphors and contributes to the application of solar cells. Therefore, the results of this research offer guidance for the design of a new NIR luminescence phosphor.

2. METHODS

2.1. Materials. Raw materials for the synthesis of RE_2MoO_6:Bi,Yb and $Gd_2Mo_{1-x}W_xO_6$:Bi,Yb nanophosphors of $Gd(NO_3)_3{\cdot}6H_2O$ (>99.95%), $(NH_4)_6Mo_7O_{24}{\cdot}4H_2O$ (>99.0%), $5(NH_4)_2O{\cdot}12WO_3{\cdot}5H_2O$ (88.0−90.0%), and HNO_3 (69.0−71.0%) were purchased from Kanto chemical Co. Inc. $Bi(NO_3)_3{\cdot}5H_2O$ (>99.5%), $Yb(NO_3)_3{\cdot}nH_2O$ (78−88%), and isopropanol (99.7+%) were purchased from Fujifilm Wako Pure Chem. Co. $Y(NO_3)_3{\cdot}6H_2O$ (99.8%) was purchased from Sigma-Aldrich. Lu_2O_3 (99.9%) was purchased from Nippon Denko Co. Ltd. Lanthanide nitrate hydrates of $Lu(NO_3)_3{\cdot}nH_2O$ and $Yb(NO_3)_3{\cdot}nH_2O$ were obtained by dissolving Lu_2O_3 and Yb_2O_3 in 1 M HNO_3 (aq) and drying it at 80 °C for several days. The hydration amounts of $Lu(NO_3)_3{\cdot}nH_2O$ and $Yb(NO_3)_3{\cdot}nH_2O$ were found to be 3.7 and 5.9, respectively, through thermogravimetry analysis. To fabricate the PDMS film, chloroform (>99.0%) was purchased from Kanto chemical Co. Inc., and PDMS (Sylgard-184) and the curing agent were purchased from Dow Corning.

2.2. Synthesis of RE_2MoO_6:Bi,Yb (RE = Gd, Y, and Lu), RE_2MoO_6, and $Gd_2Mo_{1-x}W_xO_6$:Bi,Yb (x = 0, 0.2, 0.5, 0.8, and 1) Nanophosphors. The RE_2MoO_6:Bi,Yb (REMO:Bi,Yb) nanophosphors were synthesized by using a solvothermal reaction method with isopropanol as the solvent. In a typical synthesis, a solution containing $Gd(NO_3)_3{\cdot}6H_2O$, $Y(NO_3)_3{\cdot}6H_2O$, or $Lu(NO_3)_3{\cdot}nH_2O$, $Bi(NO_3)_3{\cdot}5H_2O$, and $Yb(NO_3)_3{\cdot}nH_2O$ in isopropanol was prepared. The solution was stirred vigorously for approximately 10 min at room temperature (RT) before being transferred to a Teflon-lined autoclave vessel with a volume of 100 mL. The vessel was then heated at 220 °C for 5 h in an oven. After being cooled to room temperature, the powder was washed multiple times with water and ethanol and then collected through filtration. The resulting pale-gray powder was calcined at 850 °C for 5 h. RE_2MoO_6 (REMO: GMO, YMO, and LuMO) was synthesized by a similar process without $Bi(NO_3)_3{\cdot}5H_2O$ and $Yb(NO_3)_3{\cdot}nH_2O$. The synthesis of $Gd_2Mo_{1-x}W_xO_6$:Bi,Yb followed a similar procedure, with the exception that stoichiometric amounts of $5(NH_4)_2O{\cdot}12WO_3{\cdot}5H_2O$ and $(NH_4)_6Mo_7O_{24}{\cdot}4H_2O$ were used.

2.3. Fabrication of the PDMS and GMO:Bi,Yb Films. An appropriate amount of the GMO:Bi,Yb nanophosphor was dispersed in 3 mL of chloroform to obtain solutions of 0.5, 1, and 1.5 mg/mL. The resulting solution was then added to a mixture of 3 g of PDMS and 0.3 g of the curing agent and stirred manually until the mixture became homogeneous. The obtained pastes were deformed under vacuum conditions at 25 °C for 1 h. Subsequently, the deformed pastes were deposited

https://doi.org/10.1021/acs.jpcc.4c04814
J. Phys. Chem. C 2024, 128, 20360−20368

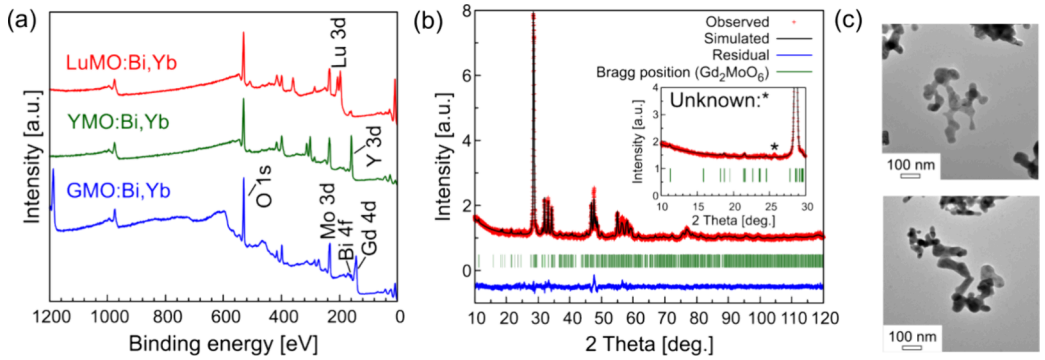

Figure 2. (a) Wide scan analysis of XPS spectra, (b) Rietveld analysis for GMO:Bi,Yb (inset: enlarged one). (c) TEM images for REMO:Bi,Yb (RE= Y (upper) and Lu (bottom)).

on a clean board and flattened to 50 μm using the doctor blade method. Finally, the board with the pastes was dried overnight at 60 °C.

2.4. Characterization. The thermal stability was measured by a thermogravimetry-differential thermal analyzer (TG-DTA8122, Rigaku). The chemical composition was analyzed by X-ray photoelectron spectroscopy (XPS, PHI5600, ULVAC-PHI Inc.) The crystal phase was determined by powder X-ray diffraction (XRD) using an X-ray diffractometer (SmartLab 3G, Rigaku) with Cu Kα radiation (λ = 1.5406 Å). The detailed structural information was refined by the Rietveld analysis technique using the RIETAN-FP program package.[33] To obtain the chemical states of each metal component, the X-ray absorption fine structure (XAFS) analysis for the W L_3-edge and Mo *K*-edge was utilized by BL12C (W L_3-edges and Mo *K*-edge) in the Photon Factory (PF) at the High Energy Accelerator Research Organization, Japan (KEK). The sample was diluted by boron nitride powder and pelleted for the measurement. The measurement mode was the transmission mode. The obtained data from XAFS were analyzed by Athena and Artemis programs.[34] The diffuse reflectance spectra (DRS) were measured by a UV−vis-NIR spectrometer (V-670, JASCO Corp.) conducted with an integrated sphere attachment. The morphology was observed by transmission electron microscopy (TEM, EM-002B, Topcon Corp.). The photoluminescence (PL) and PL excitation (PLE) spectra and quantum efficiencies were measured by a spectrofluorometer (FP-8700, JASCO Corp.) equipped with a 150 W Xe lamp as the excitation source. The temperature-dependent PL and PLE spectra and PL lifetimes of NIR luminescence due to Yb^{3+} ions were recorded by a photoluminescence spectrometer (FLS1000-SD-stm, Edinburgh Inst.) equipped with 450 W Xe lamp, and the measurement temperature was controlled by thermal stage (THMS600, Linkam Scientific Instruments). The photovoltaic performance of c-Si solar cells (LR0GC02, SHARP) with and without films was measured by a source meter (IVP-0605, Asahi spectra) under 1 sun (100 mW/cm^2, AM 1.5) of solar light simulator illumination at 25 °C.

3. RESULTS AND DISCUSSION

3.1. RE_2MoO_6:BiYb (REMO:Bi,Yb; RE = Gd, Y, and Lu) Nanophosphors. The chemical compositions of REMO:-Bi,Yb (RE=Gd, Y, and Lu) were analyzed using X-ray Photoelectron Spectroscopy (XPS) measurements, as shown in Figure 2a and Figure S1. Peaks corresponding to RE (Gd, Y, and Lu), Mo, Yb, and Bi elements were observed in each REMO:Bi,Yb. These peaks were integrated to estimate the molar ratios of RE, Bi, and Yb ions for quantitative analysis (Table S1). The maximum doping level of Bi^{3+} in REMO:Bi,Yb occurred with RE = Gd, which correlates with the ionic radius of RE and Bi^{3+}. Bi^{3+} has an ionic radius of 1.17 Å in an eight-coordination environment, and Gd^{3+} has the closest radius of 1.053 Å compared to that of Y^{3+} (1.019 Å) and Lu^{3+} (0.977 Å).[35] Therefore, Gd^{3+} is more easily substituted by Bi^{3+} in solids. Similarly, the largest doping amount of Yb^{3+} is observed with RE = Y, which can be attributed to the larger ionic radius of Yb^{3+} (0.985 Å) and the closer ionic radius of Gd^{3+}.[35] The evaluation of oxidation states was carried out based on the narrow scan analysis (Figure S1a−f) as their oxidations states were crucial factors to consider the optical properties. The peaks observed at 149 and 141 eV for Gd $4d_{3/2}$ and $4d_{5/2}$, 159 and 157 eV for Y $3d_{3/2}$ and $3d_{5/2}$, and 207 and 196 eV for Lu $4d_{3/2}$ and $4d_{5/2}$ (Figure S1a−c) were attributed to Gd^{3+}, Y^{3+}, and Lu^{3+}, respectively.[36−38] The peaks around the Y 3d spectra were deconvoluted into three peaks due to the proximity of the Bi $4f_{7/2}$ spectra to the Y 3d spectra. Two peaks at 236 and 232 eV, corresponding to Mo $3d_{3/2}$ and $3d_{5/2}$ (Figure S1d), respectively, indicated the oxidation states of Mo^{6+}.[39] The Bi $4f_{5/2}$ and $4f_{7/2}$ spectra (Figure S1e) were observed at 164 and 160 eV, respectively, implying the presence of Bi^{3+} ions.[40] The Yb 4d spectra (Figure S1f) confirmed the presence of a peak at 185 eV due to the Yb $4d_{5/2}$ of Yb^{3+} ions.[41] In addition to the XPS spectra, we evaluated the oxidation states of molybdenum using X-ray absorption near edge structure (XANES) analysis because Mo^{6+} ions are known to be easily reduced. The XANES spectra for Mo *K*-edge in REMO:Bi,Yb (Figure S2) showed the absorption edge and pre-edge around 20.009 and 19.992 keV, respectively, consistent with those of MoO_3 as a reference. Another reference sample of MoO_2 showed only an absorption edge around 20.006 keV, which was located at a lower energy due to the presence of Mo^{4+}. Furthermore, the peak positions in the derivative XANES spectra for REMO:Bi,Yb (Figure S3) were consistent with those of MoO_3. This indicated the presence of Mo^{6+} ions in all samples, confirming the absence of reductive Mo^{6+} ions in REMO:Bi,Yb.

The crystal structure was determined using the powder X-ray diffraction (XRD) method, and the observed XRD patterns were refined by Rietveld analysis as shown in Figure 2b and Figure S4. In GMO:Bi,Yb, most peaks were well fitted with the monoclinic phase of Gd_2MoO_6, while an unknown phase was observed at 26°. The peaks in YMO:Bi,Yb and LuMO:Bi,Yb were mainly attributed to the target phases of YMO and LuMO, and the peaks of $RE_2Mo_4O_{15}$ (RE= Y and Lu) and an

https://doi.org/10.1021/acs.jpcc.4c04814
J. Phys. Chem. C 2024, 128, 20360−20368

unknown phase were also observed around 18° (Figure S4). The impurity phase is almost negligible as the peaks of the impurity phase are much smaller than those of the main phase. The refined parameters are summarized in Table S2, and the reliable parameters of (R_{wp}, S) for RE = Gd, Y, and Lu were (2.98%, 3.38), (5.22%, 4.85), and (7.62%, 7.43), respectively. The S values were large due to the unknown phase and the inability to refine the oxygen positions and atomic displacement parameters, although the R_{wp} values are sufficiently low to be reliable. The reasons for the failures to refine them were as follows: (i) the samples were nanoparticles, and (ii) both of the target phases were monoclinic. Nanoparticles exhibit peak broadening in XRD patterns due to their small size, which presents a difficulty in accurately fitting each peak. The refinement of crystalline systems with low symmetry is a complex process due to the increased number of diffraction peaks and greater freedom in refinement parameters. As a consequence of the aforementioned factors, the refinement process proved to be onerous, and the S values did not decline to an adequate extent. However, the primary aim of the Rietveld refinement was to estimate the unit cell volumes (V). Accordingly, if only the lattice parameters are considered, it is acceptable not to refine all structural parameters even if this results in larger S values. The refined V values for RE = Gd, Y, and Lu were 945.4(3), 911.5(2), and 883.2(2) Å^3, respectively. They gradually reduced in the order of RE = Gd, Y, and Lu corresponding to the relationship of ionic radius of the Gd, Y, and Lu (Gd: 1.053 Å, Y: 1.019 Å, Lu: 0.977 Å). The cell parameters of RE_2MoO_6 were also refined for comparison with REMO:Bi,Yb, and the refinement and refined parameters are listed in Figure S5 and Table S3. The V values for RE_2MoO_6 were found to be 948.6(1) Å^3 for RE = Gd, 913.5(2) Å^3 for RE = Y, and 884.3(5) Å^3 for RE = Lu. The V values for RE = Gd and Y decreased due to Bi^{3+} and Yb^{3+} doping, indicating that the substitution of Yb^{3+} with a smaller ionic radius than Gd^{3+} and Y^{3+} primarily contributed to the decrease. On the other hand, there were almost no changes in V values of RE = Lu due to Bi^{3+} and Yb^{3+} doping despite their larger ionic radius compared to Lu^{3+}. This might be due to the small doping amounts of Bi^{3+} and Yb^{3+} as summarized in Table S1. TEM images of the REMO:Bi,Yb nanophosphor (Figure 2c) reveal the presence of spherical nanoparticles with a diameter of approximately 50 nm. No differences were observed between REMO:Bi,Yb nanophosphors because they belong to the same crystal structure and were synthesized under the same conditions. Based on these observations, it suggested that REMO:Bi,Yb nanophosphors have the potential to be utilized with c-Si solar cells, as they are likely to minimize the scattering of visible light in sunlight.

Figure 3 displays the diffuse reflectance spectra (DRS) for REMO:Bi,Yb. The amount of impurities in $RE_2Mo_4O_{15}$ (RE = Gd, Y, and Lu) was found to be minimal and was determined to have no significant impact on the optical properties. All samples exhibit efficient absorptions from 200 to 400 nm due to the charge transfer (CT) transition between Mo 4d orbitals and O 2p/Bi 6s hybrid orbitals. Additionally, an optical absorption was observed at around 1000 nm, which is attributed to the $^2F_{7/2} \rightarrow {}^2F_{5/2}$ transition of the Yb^{3+} ions. The band gap energy (E_g) was estimated using the Kubelka–Munk transformation and Tauc plot, calculated with eqs 1 and 2.[42]

$$(h\nu\alpha)^{1/2} = A(h\nu - E_g) \tag{1}$$

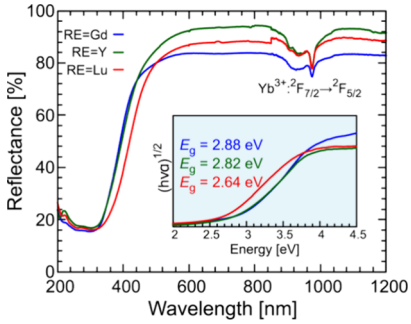

Figure 3. UV–vis-NIR diffuse reflectance spectra and Tauc plot (inset) of REMO:Bi,Yb (RE = Gd (blue), Y (dark-green), and Lu (red)).

$$\alpha = \frac{(1 - R)^2}{2R} \tag{2}$$

where $h\nu$, α, A, and R represent the photon energy, Kubelka–Munk function, absorption constant, and reflectance, respectively. The estimated E_g values for REMO:Bi,Yb with RE = Gd, Y, and Lu were 2.88, 2.82, and 2.64 eV, respectively. Those of the host matrix (RE_2MoO_6) with RE = Gd, Y, and Lu were also estimated to be 2.96, 2.88, and 2.72 eV, respectively, as shown in Figure S6, which are reasonable E_g values because the E_g values have been reported to be approximately 2.7 to 2.9 eV.[43−45] Compared to the E_g values of the host matrix, those of REMO:Bi,Yb decreased with Bi^{3+} and Yb^{3+} doping, which was attributed to the upward shift of the valence band maximum by the formation of the hybrid orbitals between the Bi 6s/O 2p orbital as observed in other Bi^{3+}-doped molybdates.[46] The E_g values decreased following the order of ionic radius for RE ions ($Gd^{3+} > Y^{3+} > Lu^{3+}$). In REMO:Bi,Yb, the E_g values were primally determined by the contribution of Bi^{3+} ions and the distance between Mo and O atoms due to the crystal field effect. The Mo 4d orbitals, forming the conduction band minimum, are affected by the crystal field splitting effect.[45] From the extended X-ray absorption fine structure (EXAFS) analysis as shown in Figure S7, the peaks at 1.38 Å for RE = Y and Lu and 1.40 Å for RE = Gd were attributed to the first coordination sphere of the O atom around the Mo atom. The shorter peak positions for RE = Y and Lu compared to RE = Gd suggest that the crystal fields around the Mo atom in RE = Y and Lu were stronger than those in RE = Gd, resulting in a reduction of the band gap due to a lower shift in the conduction band minimum. Thus, it was reasonable to observe a lower band gap of RE = Y and Lu compared to that of RE = Gd. Despite similar bond length in RE = Y and Lu, the E_g values decreased with Lu substitution. The smaller doping amount of Bi^{3+} in RE = Lu compared to RE = Y could also contribute to the decrease of E_g values.

Figure 4a displays the photoluminescence (PL) and PL excitation (PLE) spectra for REMO:Bi,Yb in the NIR region. The PL spectra under 363 nm excitation showed NIR luminescence from 950 to 1100 nm, with the strongest peak at 975 nm, attributed to the $^2F_{5/2} \rightarrow {}^2F_{7/2}$ transition of Yb^{3+} ions. The spectra exhibited five peaks at 950, 975, 1034, 1055, and 1074 nm resulting from the Stark splitting of the $^2F_{5/2}$ and $^2F_{7/2}$ levels.[47] The normalized PL spectra for REMO:Bi,Yb (RE=Gd, Y, and Lu) (Figure S8) reveal consistent NIR emission at around 1000 nm from Yb^{3+} ions. The similarity in PL spectra across REMO:Bi,Yb suggests that the crystal field

https://doi.org/10.1021/acs.jpcc.4c04814
J. Phys. Chem. C 2024, 128, 20360−20368

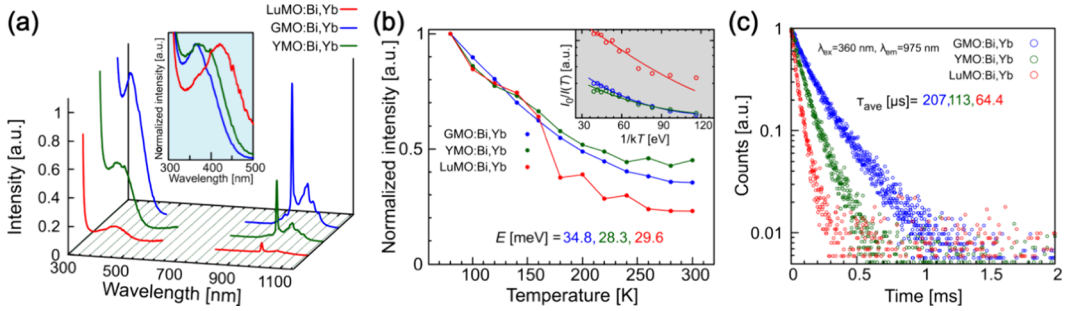

Figure 4. (a) PL·PLE spectra (λ_{ex}= 363 nm, λ_{em}= 975 nm), (b) plot of integrated PL intensity in the NIR region and Arrhenius plot (inset), and (c) decay curve (λ_{ex}= 360 nm, λ_{em}= 975 nm) at room temperature of REMO:Bi,Yb (RE = Gd, Y, and Lu).

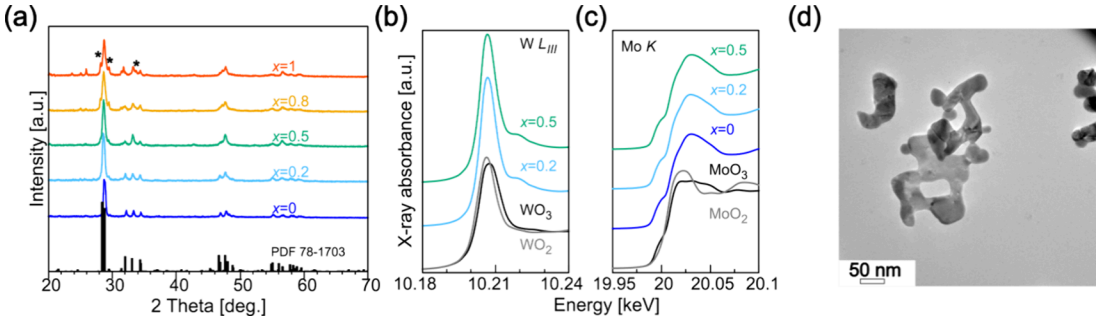

Figure 5. (a) XRD patterns (*: impurity phase of $Gd_2(WO_4)_3$) and (b, c) XANES spectra of Mo *K*- and W L_3-edge with reference samples of MoO_3, MoO_2, WO_3, and WO_2 for $Gd_2Mo_{1-x}W_xO_6$:Bi,Yb. (c) TEM image of $Gd_2Mo_{0.5}W_{0.5}O_6$:Bi,Yb.

effects on the Yb^{3+} ions are similar despite the variation in the host materials. These findings imply that Yb^{3+}-doped nanophosphors can effectively enhance the efficiency of c-Si solar cells by providing NIR emission around 1000 nm regardless of solid hosts. Under 363 nm excitation, the GMO:Bi,Yb nanophosphor exhibited the highest intensity, and the internal quantum efficiencies of REMO:Bi,Yb with RE = Gd, Y, and Lu were calculated to be 3.23, 1.84, and 0.53%, respectively. The PLE spectra monitored at 975 nm showed a broad excitation band between 300 and 500 nm for all REMO:Bi,Yb, attributed to the CT transition between Mo 4d and Bi6s/O 2p orbitals. The peak position of LuMO:Bi,Yb at 410 nm shifted toward longer wavelengths compared to those of GMO:Bi,Yb and YMO:Bi,Yb (around 363 nm). This shift was consistent with the reflectance property shown in Figure 3. To determine the origin of the order of luminescence intensity, temperature-dependent PL spectra were evaluated, as shown in Figure S9 and Figure 4b. The PL intensity for all REMO:Bi,Yb gradually decreased with increasing temperature, while peak shift or spectral shape change was not observed. Figure 4b presents plots of integrated PL intensity in the NIR regions for REMO:Bi,Yb. The temperatures at which PL intensity reduced by 50% compared to that at 80 K for REMO:Bi,Yb for RE = Gd, Y, and Lu were estimated to be 200, 221, and 170 K, respectively. The activation energy for REMO:Bi,Yb in the measured region was evaluated using the Arrhenius equations expressed by the following equation (eq 3):

$$\frac{I(T)}{I_0} = \frac{1}{1 + (\Gamma_0/\Gamma_v)\exp(-E/kT)} \tag{3}$$

where $I(T)$ and I_0 are the PL intensities at temperature T and T = 80 K, respectively, Γ_v is the radiative rate, Γ_0 is the attempt rate for the nonradiative process, E is the activation energy, and k is the Boltzmann constant (8.617×10^{-5} eV K^{-1}). The estimated E values were 34.8, 28.3, and 29.6 meV for RE = Gd, Y, and Lu, respectively. The higher E values mean that the phosphor shows less quenching with increasing temperature. However, this was not consistent with our results, suggesting that the temperature dependency did not contribute to the order of PL intensity. Consequently, the lifetime of Yb^{3+} in REMO:Bi,Yb (λ_{ex}= 363 nm, λ_{em}= 975 nm) was evaluated at room temperature as shown in Figure 4c. The decay curves were well-fitted with the equation (eq 4).

$$I(t) = A_1\exp\left(-\frac{t}{\tau_1}\right) + A_2\exp\left(-\frac{t}{\tau_2}\right) \tag{4}$$

where $\tau_{1,2}$, $A_{1,2}$, and $I(t)$ are the lifetime, decay components, and intensity at time t, respectively. In addition, the average lifetimes (τ_{ave}) were estimated by the following equation (eq 5):

$$\tau_{ave} = \frac{A_1\tau_1^2 + A_2\tau_2^2}{A_1\tau_1 + A_2\tau_2} \tag{5}$$

The fitted parameters are given in Table S4. The τ_{ave} values were 207 μs for GMO:Bi,Yb, 113 μs for YMO:Bi,Yb, and 64.4 μs for LuMO:Bi,Yb, and the values were similar to other Yb^{3+}-doped NIR phosphors, such as $CaLaNb_3O_{10}$:Yb (211 μs) and $CdMoO_4$:Yb (112 μs).[48,49] The estimated values decreased as the ionic radius of the RE site decreased. It is considered that the shortened lifetime is caused by concentration quenching. Hence, the order of luminescence intensities in the NIR spectrum for REMO:Bi,Yb nanophosphors could be attributed to concentration quenching, which tends to occur more frequently as the ionic radius decreases.

3.2. $Gd_2Mo_{1-x}W_xO_6$:Bi,Yb Nanophosphor. Because Gd_2MoO_6:Bi,Yb exhibited the highest PL intensity in RE_2MoO_6:Bi,Yb (RE = Gd, Y, and Lu), the Mo site was

https://doi.org/10.1021/acs.jpcc.4c04814
J. Phys. Chem. C 2024, 128, 20360−20368

substituted into the W atom focusing on Gd_2MoO_6:Bi,Yb. Figure 5a displays the XRD patterns for $Gd_2Mo_{1-x}W_xO_6$:Bi,Yb. The synthesis of $Gd_2Mo_{1-x}W_xO_6$:Bi,Yb was achieved with a pure phase at x = 0, 0.2, and 0.5. However, an impurity phase of $Gd_2(WO_4)_3$ was observed at x = 0.8 and 1 (marked as *), indicating that the solid solution limits of Mo and W in GMO exist between x = 0.5 and 0.8 in this solvothermal reaction method. Therefore, only $Gd_2Mo_{1-x}W_xO_6$:Bi,Yb with x = 0, 0.2, and 0.5 were subjected to further evaluation for comparison. Based on the XANES spectra of the Mo K-edge and the W L_3-edge (Figure 5b,c), the oxidation states of Mo and W atoms in $Gd_2Mo_{1-x}W_xO_6$:Bi,Yb were determined to be hexavalent. This was evidenced by the absorption edge at 20.009 keV for the Mo K-edge and 10.204 keV for the W L_3-edge, consistent with the reference samples of MoO_3 and WO_3. Additionally, from the derivative XANES spectra of the Mo K-edge and W L_3-edge (Figure S10), the peak positions agreed well with MoO_3 or WO_3, not with MoO_2 or WO_2. Therefore, the formation of the solid solution with Mo and W did not alter their oxidation states, and there was no need to consider the existence of reductive states of Mo^{6+} and W^{6+}. The TEM image in Figure 5d shows that $Gd_2Mo_{0.5}W_{0.5}O_6$:Bi,Yb has a spherical morphology of 50 nm, consistent with that of GMO:Bi,Yb. Thus, the morphology is not affected by W substitution, and $Gd_2Mo_{1-x}W_xO_6$:Bi,Yb is expected to suppress the visible light scattering as well as the REMO:Bi,Yb nanophosphor.

Figure 6 displays the DRS spectra for $Gd_2Mo_{1-x}W_xO_6$:Bi,Yb (x = 0, 0.2, and 0.5), which exhibit absorptions from 200 to

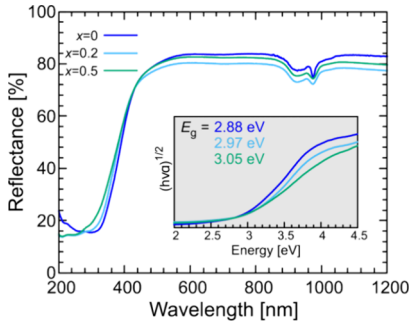

Figure 6. UV−vis-NIR diffuse reflectance spectra and Tauc plot (inset) of $Gd_2Mo_{1-x}W_xO_6$:Bi,Yb (blue: x = 0, light blue: x = 0.2, green: x = 0.5).

300 nm due to CT transitions between Bi 6s/O 2p orbitals and Mo 4d or W 5d orbitals. Additionally, absorption due to the Yb^{3+} ions was observed in the NIR region around 1000 nm. Furthermore, a shift of the absorption edge toward shorter wavelengths was observed as x increased. The estimated values of E_g, obtained from eqs 1 and 2, were 2.88, 2.97, and 3.05 eV for x values of 0, 0.2, and 0.5, respectively. The increase of E_g values could be attributed to the enhanced contribution of the W 5d orbital, which is located at a higher energy level than the Mo 4d orbitals.[43,50] These results indicated that the absorption property can be tuned by the ratio of the W and Mo amount.

Figure 7a shows the PLE spectra for the $Gd_2Mo_{1-x}W_xO_6$:Bi,Yb (x = 0, 0.2, and 0.5) monitored at an NIR luminescence of 975 nm. The discrepancy between the PLE spectra of the GMO:Bi,Yb spectrum and Figure 4a is due to the presence or absence of the detector correction. In the PLE spectra for $Gd_2Mo_{1-x}W_xO_6$:Bi,Yb, no correction allowed for the deconvolution of the excitation band. The PLE spectra

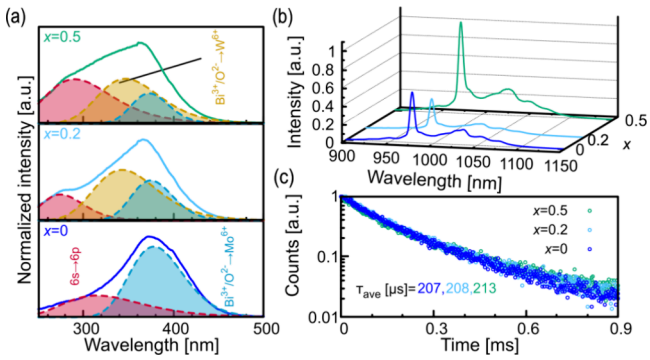

Figure 7. (a) Normalized PLE spectra (λ_{em}= 975 nm), (b) PL spectra, and (c)decay curve (λ_{ex}= 360 nm, λ_{em}= 975 nm) for $Gd_2Mo_{1-x}W_xO_6$:Bi,Yb (blue: x = 0, light blue: x = 0.2, and green: x = 0.5).

for Gd_2MoO_6:Bi,Yb were deconvoluted into two bands, attributed to the 6s → 6p transition of Bi^{3+} ions and CT transition between Bi 6s/O 2p hybrid orbitals and Mo 4d orbitals, respectively, peaking at 303 and 380 nm.[21] In comparison, the PLE spectra for $Gd_2Mo_{1-x}W_xO_6$:Bi,Yb (x = 0.2 and 0.5) were deconvoluted into three bands peaking at approximately 283, 342, and 377 nm. Based on the attribution of PLE spectra in GMO:Bi,Yb, the bands at 283 and 377 nm should be attributed to 6s → 6p of Bi^{3+} and the CT transition, respectively, as these band positions would not show drastic changes with W substitution. Therefore, the band at 342 nm was due to the CT transitions between the Bi 6s/O 2p hybrid orbitals and the W 5d orbitals. From the PL spectra for all $Gd_2Mo_{1-x}W_xO_6$:Bi,Yb under 363 nm excitation (Figure 7b), NIR luminescence was observed from 900 to 1150 nm due to the 4f-4f transitions of Yb^{3+} ions. In $Gd_2Mo_{1-x}W_xO_6$:Bi,Yb, $Gd_2Mo_{0.5}W_{0.5}O_6$:Bi,Yb exhibited the highest PL intensity, with an increase of up to 1.7 times compared to the GMO:Bi,Yb, The internal quantum efficiencies for $Gd_2Mo_{1-x}W_xO_6$:Bi,Yb (x = 0, 0.2, and 0.5) under 363 nm excitation were found to be 3.23, 2.55, and 3.81%, respectively. The results indicate that the concentration of the W^{6+} ion has an effect on the luminescence intensity. From the normalized PL spectra for $Gd_2Mo_{1-x}W_xO_6$:Bi,Yb (x = 0, 0.2, and 0.5) as displayed in Figure S11, there was no shift or spectral shape difference, indicating the similarity of the crystal field effects on the Yb^{3+} ions. Figure 7c presents the decay curve for $Gd_2Mo_{1-x}W_xO_6$:Bi,Yb (λ_{ex}= 363 nm, λ_{em}= 975 nm) at room temperature. The decay curve follows eq 5, and the fitted values are summarized in Table S5. The τ_{ave} values remained consistent across different W concentrations (x = 0:207, 0.2:208, and 0.5:213 μs), which mean that there were no changes in radiative transition rate of Yb^{3+}. Therefore, the variation in PL intensity observed in $Gd_2Mo_{1-x}W_xO_6$:Bi,Yb might be attributed to the energy transfer processes from CT transitions in $Gd_2Mo_{1-x}W_xO_6$:Bi to Yb^{3+}.

3.3. Current−Voltage (*I*−*V*) Characteristics of the GMO:Bi,Yb Nanophosphor. In this study, we focused on the GMO:Bi,Yb nanophosphor due to its strong luminescence intensity and possibility up to long wavelengths. Figure 8a displays the in-line transmittance spectra for the PDMS/GMO:Bi,Yb film, as well as the PDMS film put onto quartz glass as the reference. The PDMS film exhibited high transmittance, approximately 92%, while it showed a reduction of transmittance from near-UV (NUV) to the NIR region of

https://doi.org/10.1021/acs.jpcc.4c04814
J. Phys. Chem. C 2024, 128, 20360−20368

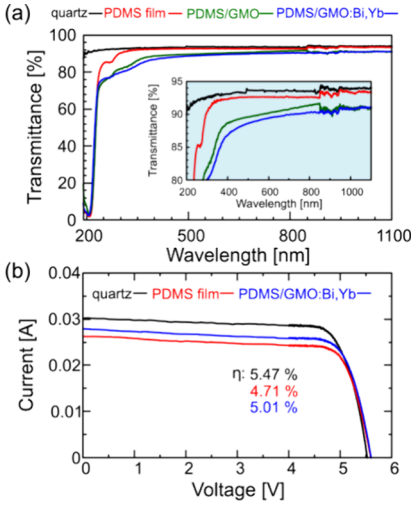

Figure 8. (a) Transmittance spectra of quartz, PDMS film, and PDMS/GMO:Bi,Yb film. (c) $I-V$ curve for c-Si solar cells with the PDMS film and c-Si/PDMS/GMO:Bi,Yb film.

approximately 1% compared to quartz. This reduction should not significantly impact conversion efficiency, although strong absorption was observed in the wavelength region below 250 nm due to the intrinsic absorption of PDMS. It suggests that the GMO:Bi,Yb nanophosphor with absorption over 250 nm would be beneficial if using PDMS as a polymer resin to mitigate the effects of absorption of PDMS. Compared to the PDMS film, the PDMS/GMO:Bi,Yb film displayed a reduction in transmittance of 2−4% in the visible to NIR region due to scattering and absorption by GMO:Bi,Yb nanophosphors. Additionally, the transmittance in the NUV region around 300 nm decreased further by approximately 10% due to the LMCT transition in GMO:Bi,Yb. Therefore, it was anticipated that the PDMS/GMO:Bi,Yb film would enhance the properties of c-Si solar cells. Figure S12 shows a photograph of the PDMS/GMO:Bi,Yb film, which was highly transparent due to the absorption of GMO:Bi,Yb only in the UV region and its nanoscale size with an average thickness of 312 μm. Figure 8b illustrates the current−voltage ($I-V$) characteristic of c-Si with and without a film. The conversion efficiency (η) of bare c-Si, PDMS, and PDMS/GMO:Bi,Yb film was 5.47, 4.71, and 5.01%, respectively. The PDMS film led to a 0.8% decrease in η value compared to the bare state, attributed to the scattering of the light, indicating that film deposition conditions, such as film thickness, are necessary to be optimized. Although there is still room for improvement in the deposition conditions, the η value of the PDMS/GMO:Bi,Yb film is 0.3% higher than that of the PDMS film. This improvement was attributed to the contribution of the GMO:Bi,Yb nanophosphor. Moreover, the conversion efficiency was evaluated by varying the concentrations of the GMO:Bi,Yb chloroform solution. The η values for 0.5, 1.0, and 1.5 mg/mL were found to be 4.94, 5.01, and 4.42%, respectively, with the highest efficiency observed at a concentration of 1.0 mg/mL.

4. CONCLUSIONS

In this research, RE_2MoO_6:Bi,Yb (RE = Gd, Y, Lu) and $Gd_2Mo_{1-x}W_xO_6$:Bi,Yb (x = 0−0.5) nanophosphors were successfully synthesized using a solvothermal reaction method. The RE_2MoO_6:Bi,Yb nanophosphors exhibited peaks corresponding to the Yb^{3+} and Bi^{3+} ions in XPS spectra, suggesting successful substitution in the host matrix. The TEM images revealed that all samples had spherical nanoparticles with a diameter of approximately 50 nm, and no difference was observed among them. Furthermore, the RE_2MoO_6:Bi,Yb nanophosphor exhibited absorption in the UV region and high reflectivity in the visible region. A broad excitation band attributed to the CT transition between the Bi 6s/O 2p and Mo 4d orbitals was observed. Additionally, upon excitation at 364 nm, the RE_2MoO_6:Bi,Yb nanophosphor displayed NIR luminescence around 1000 nm due to the 4f-4f transition of Yb^{3+} ions, and Gd_2MoO_6:Bi,Yb exhibited the highest luminescence intensity. By tuning the chemical compositions of $Gd_2Mo_{1-x}W_xO_6$:Bi,Yb nanophosphors, the band edge in reflectance spectra shifted toward a shorter wavelength with increasing x values, and also the blue shift of peak position was observed in the PLE spectra. The PL intensity at 975 under 363 nm excitation was the highest in $Gd_2Mo_{0.5}W_{0.5}O_6$:Bi,Yb. The PDMS/GMO:Bi,Yb film showed a 0.5% increase in conversion efficiency compared to the PDMS film, indicating that the GMO:Bi,Yb nanophosphor played a significant role in the enhancement. This study suggests that other phosphors also improve the conversion efficiency of c-Si solar cells, and the combination of GMO:Bi,Yb nanophosphors could help address global energy issues.

■ ASSOCIATED CONTENT

Supporting Information

The Supporting Information is available free of charge at https://pubs.acs.org/doi/10.1021/acs.jpcc.4c04814.

XPS spectra, XANES spectra, Rietveld refinement, Tauc plot, EXAFS, PL spectra, and photographs (PDF)

■ AUTHOR INFORMATION

Corresponding Author

Takuya Hasegawa − *Institute of Multidisciplinary Research for Advanced Material (IMRAM), Tohoku University, Sendai 980-8577, Japan;* orcid.org/0000-0002-6170-5632; Email: hase@tohoku.ac.jp

Authors

Taisei Hangai − *Institute of Multidisciplinary Research for Advanced Material (IMRAM), Tohoku University, Sendai 980-8577, Japan;* orcid.org/0009-0002-8165-0568

Jian Xu − *International Center for Young Scientists (ICYS), National Institute for Materials Science (NIMS), Tsukuba, Ibaraki 305-0044, Japan;* orcid.org/0000-0002-1040-5090

Takayuki Nakanishi − *Advanced Phosphor Group, National Institute for Materials Science (NIMS), Tsukuba, Ibaraki 305-0044, Japan;* orcid.org/0000-0003-3412-2842

Takashi Takeda − *Advanced Phosphor Group, National Institute for Materials Science (NIMS), Tsukuba, Ibaraki 305-0044, Japan;* orcid.org/0000-0003-2510-4562

Tomoyo Goto − *SANKEN (The Institute of Scientific and Industrial Research), Osaka University, Ibaraki, Osaka 567-0047, Japan; Institute for Advanced Co-Creation Studies, Osaka University, Suita, Osaka 565-0871, Japan;* orcid.org/0000-0003-1362-6750

Yasushi Sato − *Department of Chemistry, Faculty of Science, Okayama University of Science, Okayama 700-0005, Japan;* orcid.org/0000-0001-5132-0301

https://doi.org/10.1021/acs.jpcc.4c04814
J. Phys. Chem. C 2024, 128, 20360−20368

Ayahisa Okawa − *Institute of Multidisciplinary Research for Advanced Material (IMRAM), Tohoku University, Sendai 980-8577, Japan*

Shu Yin − *Institute of Multidisciplinary Research for Advanced Material (IMRAM), Tohoku University, Sendai 980-8577, Japan; Advanced Institute for Materials Research (WPI-AIMR), Tohoku University, Sendai 980-8577, Japan;* orcid.org/0000-0002-5449-4937

Complete contact information is available at: https://pubs.acs.org/10.1021/acs.jpcc.4c04814

Notes

The authors declare no competing financial interest.

■ ACKNOWLEDGMENTS

This work was supported by research granted from The Murata Science Foundation; JSPS KAKENHI (grant numbers 20K15106, 22K05264, and 20H00297); Feasibility Study for Young Researchers (FS) in "Crossover Alliance to Create the Future with People, Intelligence and Materials", MEXT, Japan; the establishment of university fellowships towards the creation of science technology innovation, grant JPMJFS2102; and NIMS Joint Research Hub Program. The XAFS measurements were performed with the beamlines of BL12C at the PF with the approval of the High Energy Accelerator Research Organization (KEK) (2020P001 and 2021G608). The XPS measurements were performed with the TAGEN-CAF.

■ REFERENCES

(1) Zhou, X.; Geng, W.; Li, J.; Wang, Y.; Ding, J.; Wang, Y. An Ultraviolet−Visible and Near-Infrared-Responded Broadband NIR Phosphor and Its NIR Spectroscopy Application. *Adv. Opt. Mater.* **2020**, *8* (8), No. 1902003.

(2) Dong, L.; Zhang, L.; Xu, Y.; Yin, S.; You, H. Efficient Red and Broadband Near-Infrared Luminescence in Mn^{2+}/Yb^{3+}-Doped Phosphate Phosphor. *J. Am. Ceram. Soc.* **2021**, *104* (8), 4109−4118.

(3) Yao, L.; Shao, Q.; Han, S.; Liang, C.; He, J.; Jiang, J. Enhancing Near-Infrared Photoluminescence Intensity and Spectral Properties in Yb^{3+} Codoped $LiScP_2O_7:Cr^{3+}$. *Chem. Mater.* **2020**, *32* (6), 2430−2439.

(4) He, S.; Zhang, L.; Wu, H.; Wu, H.; Pan, G.; Hao, Z.; Zhang, X.; Zhang, L.; Zhang, H.; Zhang, J. Efficient Super Broadband NIR $Ca_2LuZr_2Al_3O_{12}:Cr^{3+},Yb^{3+}$ Garnet Phosphor for Pc-LED Light Source toward NIR Spectroscopy Applications. *Adv. Opt. Mater.* **2020**, *8* (6), No. 1901684.

(5) Qiao, J.; Zhou, G.; Zhou, Y.; Zhang, Q.; Xia, Z. Divalent Europium-Doped near-Infrared-Emitting Phosphor for Light-Emitting Diodes. *Nat. Commun.* **2019**, *10* (1), 5267.

(6) Liu, G.; Molokeev, M. S.; Xia, Z. Structural Rigidity Control toward Cr^{3+}-Based Broadband Near-Infrared Luminescence with Enhanced Thermal Stability. *Chem. Mater.* **2022**, *34* (3), 1376−1384.

(7) Yuan, L.; Jin, Y.; Wu, H.; Deng, K.; Qu, B.; Chen, L.; Hu, Y.; Liu, R. S. Ni^{2+}-Doped Garnet Solid-Solution Phosphor-Converted Broadband Shortwave Infrared Light-Emitting Diodes toward Spectroscopy Application. *ACS Appl. Mater. Interfaces* **2022**, *14* (3), 4265−4275.

(8) Watanabe, R.; Iso, Y.; Isobe, T. Electrophoretically Deposited $Y_2O_3:Bi^{3+},Yb^{3+}$ Nanosheet Films as Spectral Converters for Crystalline Silicon Solar Devices. *ACS Appl. Nano Mater.* **2019**, *2* (6), 4009−4017.

(9) Trejgis, K.; Maciejewska, K.; Bednarkiewicz, A.; Marciniak, L. Near-Infrared-to-Near-Infrared Excited-State Absorption in $LaPO_4:Nd^{3+}$ Nanoparticles for Luminescent Nanothermometry. *ACS Appl. Nano Mater.* **2020**, *3* (5), 4818−4825.

(10) Chen, G.; Ohulchanskyy, T. Y.; Kachynski, A.; Ågren, H.; Prasad, P. N. Intense Visible and Near-Infrared Upconversion Photoluminescence in Colloidal $LiYF_4:Er^{3+}$ Nanocrystals under Excitation at 1490 Nm. *ACS Nano* **2011**, *5* (6), 4981−4986.

(11) Li, J.; Chen, L.; Hao, Z.; Zhang, X.; Zhang, L.; Luo, Y.; Zhang, J. Efficient Near-Infrared Downconversion and Energy Transfer Mechanism of Ce^{3+}/Yb^{3+} Codoped Calcium Scandate Phosphor. *Inorg. Chem.* **2015**, *54* (10), 4806−4810.

(12) Yadav, R. V.; Yadav, R. S.; Bahadur, A.; Singh, A. K.; Rai, S. B. Enhanced Quantum Cutting via Li^+ Doping from a Bi^{3+}/Yb^{3+}-Codoped Gadolinium Tungstate Phosphor. *Inorg. Chem.* **2016**, *55* (21), 10928−10935.

(13) Liang, Y. J.; Liu, F.; Chen, Y. F.; Wang, X. J.; Sun, K. N.; Pan, Z. New Function of the Yb^{3+} Ion as an Efficient Emitter of Persistent Luminescence in the Short-Wave Infrared. *Light: Sci. Appl.* **2016**, *5* (7), e16124−e16124.

(14) Li, K.; Van Deun, R. Novel Intense Emission-Tunable $Li_{1.5}La_{1.5}WO_6:Mn^{4+},Nd^{3+},Yb^{3+}$ Material with Good Luminescence Thermal Stability for Potential Applications in c-Si Solar Cells and Plant-Cultivation Far-Red-NIR LEDs. *ACS Sustain. Chem. Eng.* **2019**, *7* (19), 16284−16294.

(15) Ward, M. D. Mechanisms of Sensitization of Lanthanide(III)-Based Luminescence in Transition Metal/Lanthanide and Anthracene/Lanthanide Dyads. *Coord. Chem. Rev.* **2010**, *254* (21−22), 2634−2642.

(16) Fan, F.; Liu, F.; Yu, S.; Wu, J.; Zhang, J.; Wang, T.; Li, Y.; Zhao, L.; Qiang, Q.; Chen, W. Efficient Near-Infrared Luminescence and Energy Transfer Mechanism in $Ca_3Al_2O_6$: Ce^{3+}, Yb^{3+} Phosphors. *J. Lumin.* **2022**, *241*, No. 118511.

(17) Wu, D.; Dong, X.; Xiao, W.; Hao, Z.; Zhang, J. Efficient Visible-to-NIR Spectral Conversion for Polycrystalline Si Solar Cells and Revisiting the Energy Transfer Mechanism from Ce^{3+} to Yb^{3+} in $Lu_3Al_5O_{12}$ Host. *Inorg. Chem.* **2019**, *58* (1), 234−242.

(18) Sharma, S. K.; Bettinelli, M.; Carrasco, I.; Karlsson, M. Influence of Ce3+ Concentration on the Thermal Stability and Charge-Trapping Dynamics in the Green Emitting Phosphor $CaSc_2O_4:Ce^{3+}$. *J. Phys. Chem. C* **2017**, *121* (41), 23096−23103.

(19) Wang, X.; Wang, Y. Synthesis, Structure, and Photoluminescence Properties of Ce^{3+}-Doped $Ca_2YZr_2Al_3O_{12}$: A Novel Garnet Phosphor for White LEDs. *J. Phys. Chem. C* **2015**, *119* (28), 16208−16214.

(20) López-Pacheco, G.; López-Juárez, R.; Villafuerte-Castrejón, M. E.; Falcony, C.; Barrera-Calva, E.; González, F. Luminescence Properties of Yb^{3+}-Doped $SrTiO_3$: The Significance of the Oxygen−Titanium Charge Transfer State on Photon Downshifting. *Dalton Trans.* **2019**, *48* (31), 11889−11896.

(21) Hangai, T.; Hasegawa, T.; Xu, J.; Nakanishi, T.; Takeda, T.; Nakano, K.; Hongo, K.; Maezono, R.; Goto, T.; Sato, Y.; et al. Key Role of Metal-to-Metal Charge Transfer Transition between Mo^{6+} and Bi^{3+} for Enhancement in NIR Luminescence of Gd_2MoO_6:Bi, Yb Nanophosphor. *J. Phys. Chem. C* **2024**, *128* (8), 3351−3360.

(22) Gueymard, C. A.; Myers, D.; Emery, K. Proposed Reference Irradiance Spectra for Solar Energy Systems Testing. *Sol. Energy* **2002**, *73* (6), 443−467.

(23) McKittrick, J.; Shea-Rohwer, L. E. Review: Down Conversion Materials for Solid-State Lighting. *J. Am. Ceram. Soc.* **2014**, *97* (5), 1327−1352.

(24) Hemmer, E.; Benayas, A.; Légaré, F.; Vetrone, F. Exploiting the Biological Windows: Current Perspectives on Fluorescent Bioprobes Emitting above 1000 Nm. *Nanoscale Horiz.* **2016**, *1* (3), 168−184.

(25) Hasegawa, T.; Ueda, T.; Asakura, Y.; Yin, S. Cerium(III) Niobate Layered Perovskites: Abnormal Optical Absorption Modulations by Tuning of B-Site Composition and Perovskite Layer Charge Control. *Inorg. Chem.* **2022**, *61* (50), 20636−20646.

(26) Hasegawa, T.; Kim, S. W.; Abe, Y.; Muto, M.; Watanabe, M.; Kaneko, T.; Uematsu, K.; Ishigaki, T.; Toda, K.; Sato, M.; et al. Determination of the Crystal Structure and Photoluminescence Properties of $NaEu_{1-x}Gd_x(MoO_4)_2$ Phosphor Synthesized by a Water-Assisted Low-Temperature Synthesis Technique. *RSC Adv.* **2017**, *7* (40), 25089−25094.

(27) Kitagawa, Y.; Ueda, J.; Arai, K.; Kageyama, H.; Tanabe, S. Difference of Eu^{3+} Luminescent Properties in YOCl and YOBr Oxyhalide Hosts. *J. Appl. Phys.* **2021**, *129* (18), No. 183104.
(28) Ueda, J.; Minowa, T.; Xu, J.; Tanaka, S.; Nakanishi, T.; Takeda, T.; Tanabe, S. Highly Thermal Stable Broadband Near-Infrared Luminescence in Ni^{2+}-Doped $LaAlO_3$ with Charge Compensator. *ACS Appl. Opt. Mater.* **2023**, *1* (6), 1128−1137.
(29) Li, X.; Sun, Z.; Jia, M.; Liu, G.; Fu, Z.; Wei, Y.; Sheng, T.; Li, P. Investigation of the Luminescent Mechanism in Eu^{3+}-Doped Ln_2MoO_6 (Ln^{3+}= La^{3+}, Gd^{3+}, Y^{3+}) Phosphors for Warm WLED. *Mater. Res. Bull.* **2020**, *124*, No. 110767.
(30) Ren, X.; Gao, J.; Shi, H.; Huang, L.; Zhao, S.; Xu, S. A Highly Sensitive All-Fiber Temperature Sensor Based on the Enhanced Green Upconversion Luminescence in Lu_2MoO_6:Er^{3+}/Yb^{3+} Phosphors by Co-Doping Li^+ Ions. *Optik (Stuttg)* **2021**, *227*, No. 166084.
(31) Hämmer, M.; Janka, O.; Bönnighausen, J.; Klenner, S.; Pöttgen, R.; Höppe, H. A. On the Phosphors $Na_5M(WO_4)_4$ (M = Y, La−Nd, Sm−Lu, Bi) − Crystal Structures, Thermal Decomposition, and Optical and Magnetic Properties. *Dalton Trans.* **2020**, *49* (24), 8209−8225.
(32) Zheng, J.; Mehrvarz, H.; Liao, C.; Bing, J.; Cui, X.; Li, Y.; Gonçales, V. R.; Lau, C. F. J.; Lee, D. S.; Li, Y.; et al. Large-Area 23%-Efficient Monolithic Perovskite/Homojunction-Silicon Tandem Solar Cell with Enhanced Uv Stability Using down-Shifting Material. *ACS Ene. Lett.* **2019**, *4* (11), 2623−2631.
(33) Izumi, F.; Momma, K. Three-Dimensional Visualization in Powder Diffraction. *Solid State Phenom.* **2007**, *130*, 15−20.
(34) Ravel, B.; Newville, M. ATHENA, ARTEMIS, HEPHAESTUS: Data Analysis for X-Ray Absorption Spectroscopy Using IFEFFIT. *J. Synchrotron Radiat.* **2005**, *12* (4), 537−541.
(35) Shannon, R. D. Revised Effective Ionic Radii and Systematic Studies of Interatomie Distances in Halides and Chaleogenides. *Acta Crystallogr.* **1976**, *32*, 751.
(36) Singh, B. P.; Parchur, A. K.; Ningthoujam, R. S.; Ansari, A. A.; Singh, P.; Rai, S. B. Influence of Gd^{3+} Co-Doping on Structural Property of $CaMoO_4$:Eu Nanoparticles. *Dalton Trans.* **2014**, *43* (12), 4770−4778.
(37) Kallel, W.; Bouattour, S.; Ferreira, L. F. V.; Botelho do Rego, A. M. Synthesis, XPS and Luminescence (Investigations) of Li^+ and/or Y^{3+} Doped Nanosized Titanium Oxide. *Mater. Chem. Phys.* **2009**, *114* (1), 304−308.
(38) Hu, B.; Sun, K.; Wang, J.; Xu, J.; Liu, B.; Zhang, J.; Yang, Y.; Du, B. High Dielectric Performance of (Nb^{5+}, Lu^{3+}) Co-Doped TiO_2 Ceramics in a Broad Temperature Range. *Mater. Lett.* **2020**, *271*, No. 127838.
(39) Zhang, X.; Xu, D.; Huang, D.; Liu, F.; Xu, K.; Wang, H.; Zhang, S. Enhanced Visible-Light-Driven Photocatalytic Activities of $LiInO_2$ by Mo^{6+}-Doping Strategy. *J. Am. Ceram. Soc.* **2017**, *100* (7), 2781−2789.
(40) Zhang, S.; Zhang, S.; Song, L. Super-High Activity of Bi^{3+} Doped Ag_3PO_4 and Enhanced Photocatalytic Mechanism. *Appl. Catal. B Environ.* **2014**, *152*−*153*, 129−139.
(41) Reszczyńska, J.; Grzyb, T.; Sobczak, J. W.; Lisowski, W.; Gazda, M.; Ohtani, B.; Zaleska, A. Visible Light Activity of Rare Earth Metal Doped (Er^{3+}, Yb^{3+} or Er^{3+}/Yb^{3+}) Titania Photocatalysts. *Appl. Catal. B Environ.* **2015**, *163*, 40−49.
(42) Hasegawa, T.; Abe, Y.; Koizumi, A.; Ueda, T.; Toda, K.; Sato, M. Bluish-White Luminescence in Rare-Earth-Free Vanadate Garnet Phosphors: Structural Characterization of $LiCa_3MV_3O_{12}$ (M = Zn and Mg). *Inorg. Chem.* **2018**, *57* (2), 857−866.
(43) Xue, J.; Li, H.; Noh, H. M.; Choi, B. C.; Park, S. H.; Jeong, J. H.; Kim, J. H. Molybdenum Substitution Induced Luminescence Enhancement in $Gd_2W_{1-x}Mo_xO_6$:Eu^{3+} Phosphors for near Ultraviolet Based Solid-State Lighting. *J. Lumin.* **2018**, *202*, 97−106.
(44) Li, H.; Yang, H. K.; Jeong, J. H.; Jang, K.; Lee, H. S.; Yi, S. S. Sol−Gel Synthesis, Structure and Photoluminescence Properties of Nanocrystalline Lu_2MoO_6:Eu^{3+}. *Mater. Res. Bull.* **2011**, *46* (9), 1352−1358.
(45) Li, H.; Zhang, S.; Zhou, S.; Cao, X.; Zheng, Y. Crystalline Size Effect on the Energy Transfer from Mo-O Groups to Eu^{3+} Ions in R_2MoO_6:Eu (R) La, Gd, and Y) Crystals. *J. Phys. Chem. C* **2009**, *113* (30), 13115−13120.
(46) Colmont, M.; Boutinaud, P.; Latouche, C.; Massuyeau, F.; Huvé, M.; Zadoya, A.; Jobic, S. Origin of Luminescence in La_2MoO_6 and $La_2Mo_2O_9$ and Their Bi-Doped Variants. *Inorg. Chem.* **2020**, *59* (5), 3215−3220.
(47) Zhang, Y.; Xin, J.; Zheng, H.; Zhao, Z.; Zhang, J.; Yang, Y.; Zheng, S.; Zhao, R.; Ding, B. Yb^{3+} Doping Monoclinic Lu_2WO_6: Near-Infrared Emission and Energy-Transfer Luminescence Mechanism. *J. Phys. Chem. C* **2018**, *122* (37), 21607−21616.
(48) Guzik, M.; Tomaszewicz, E.; Guyot, Y.; Legendziewicz, J.; Boulon, G. Spectroscopic Properties, Concentration Quenching and Yb^{3+} Site Occupations in Vacancied Scheelite-Type Molybdates. *J. Lumin.* **2016**, *169*, 755−764.
(49) Lu, Y.; Li, Y.; Qin, L.; Huang, Y.; Qin, C.; Tsuboi, T.; Huang, W. Efficient Conversion from UV Light to Near-IR Emission in Yb^{3+}-Doped Triple-Layered Perovskite $CaLaNb_3O_{10}$. *Mater. Res. Bull.* **2015**, *64*, 425−431.
(50) Jiao, M.; Yu, Y.; Liu, M.; Yang, C.; Xu, Q.; You, H. Mo^{6+} Substitution Induced Band Structure Regulation and Efficient near-UV-Excited Red Emission in NaLaMg(W,Mo)O_6:Eu Phosphor. *Opt. Mater. Express* **2017**, *7* (7), 2660−2671.

https://doi.org/10.1021/acs.jpcc.4c04814
J. Phys. Chem. C 2024, 128, 20360−20368